Local structure and magnetic properties of B2- and B20-like ultrathin Mn films grown on Si(001)

S. Kahwaji, R. A. Gordon, E. D. Crozier, and T. L. Monchesky

Local structure and magnetic properties of B2 and B20-like ultrathin MnSi films grown on Si(001)

S. Kahwaji[1], R. A. Gordon[2], E. D. Crozier[2], T. L. Monchesky[1]

[1] Department of Physics and Atmospheric Science, Dalhousie University, Halifax, NS, Canada B3H 3J5

[2] Department of Physics, Simon Fraser University, Burnaby, BC, Canada V5A 1S6

Abstract

The structural and magnetic properties of ultrathin Mn layers deposited onto Si(001) by molecular beam epitaxy (MBE) at low temperature are reported. X-ray absorption fine structure (XAFS) studies reveal that the structure of the silicide layer that forms depends on the growth temperature of the capping layer. A capping layer grown at 200 ºC on 0.35 monolayer (ML) Mn results in a metastable MnSi phase with a B2-like (CsCl) structure, whereas a cap grown at room temperature on 0.5 ML followed by annealing at 200 °C produces a lower coordinated MnSi phase with a B20-like structure. Increasing the Mn thickness from 0.5 to 4 monolayers does not trigger a structural transformation but drives the structure closer to MnSi-B20. The sample with B2-like structure has the largest Mn magnetic moment of $0.33\mu_B$/Mn at T=2 K, and a Curie temperature T_C above 250 K. MnSi-B20 layers showed lower moments and much lower T_C's, in-line with those reported for MnSi-B20 thin films.

1. Introduction

Given the technological importance of Si, it is important for the field of spintronics to identify possible magnetic materials that are compatible with it. The observation of a high Curie temperature $T_C > 400\text{K}$ in Mn^+ ion implanted Si[1] and in sputtered Mn-doped Si[2] led the search for dilute magnetic semiconductors based on this material system. Structural analysis of dilute Mn_xSi_{1-x} attributed the high T_C to the co-existence of small Mn clusters and a nanocrystalline $MnSi_{1.7}$ phase.[3] A more detailed study later found that $MnSi_{1.7}$ likely had an ordering temperature closer to a bulk T_C = 47 K and other nanocrystalline phases were responsible for the high T_C.[4] Depending on Mn concentration and thermal manipulation during sample growth, precipitates with various Si:Mn phases[5, 6] or nanocrystallites with defect MnSi structures[7] are produced. In addition, the size and shape of the ensuing precipitates are also influenced by the growth conditions and structures such as $MnSi_{1.7}$ nanospheres[8] and Mn_xSi_{1-x} nanopipes[9] have been reported. However, the report of $T_C > 400$ ºC [1,2,4,8] is surprising given the low T_C of all known bulk Mn-Si phases, which include Mn_3Si, an antiferromagnet (AF) with a Néel temperature T_N =23 K,[10,11] Mn_5Si_3 (AF, T_N =99 K),[12] MnSi (T_C =29.5 K) which is a helical magnet (HM),[13] and the higher manganese silicide $MnSi_{1.7}$ family (HM, $T_C \sim 43$ K).[14, 15] One model attempts to explain the high T_C in this condensed magnetic semiconductor as due to an enhancement of the coupling between Mn spins in the Si matrix due to spin-fluctuations in the itinerant $MnSi_{1.7}$ precipitates.[16]

A second proposal to create high T_C ferromagnetic Mn-Si systems is to stabilize new metastable phases with epitaxially induced strain. While bulk MnSi has a B20 crystal structure with a lattice constant $a = 0.4558$ nm, which has a 3% mismatch to the Si(111) surface for MnSi[110] || Si[112], the B20 phase is much less favorable on Si(001) owing to a 16% lattice mismatch. Density functional theory (DFT) calculations[17,18] predict that MnSi with a B2 structure is energetically favorable relative to the B20 phase when grown on Si(001). According to these calculations, Mn in a

cubic MnSi-B2 has 8 nearest-neighbor Si atoms located at 2.37Å and 6 next-nearest-neighbor Mn atoms at 2.74Å. However, a distorted MnSi-B2 structure is expected to grow on Si(001) due to a 2% lattice mismatch. This mismatch is the same as that observed experimentally for FeSi-B2 and CoSi-B2 stabilized on Si(111).[19,20] Furthermore, the cited DFT calculations predict a ferromagnetic ordering in films of MnSi-B2/Si(001) with a Mn coverage up to 3 ML, and[18] a T_C up to 328 K for the 2 ML MnSi-B2 film. Motivated by these findings and by our previous discovery of a B2-type structure in a submonolayer of Mn/Si(001),[21] we explored the possibility of stabilizing thicker layers of MnSi-B2/Si(001) grown by low-temperature molecular beam epitaxy (MBE). In this paper we present structural and magnetic characterization of MnSi ultrathin films ranging in thickness from 0.35 – 4 ML.

2. Film growth and structural characterization

We used MBE to grow ultrathin MnSi films in ultra high vacuum conditions (base pressure < $5x10^{-11}$ Torr). All samples were grown on boron-doped (1 – 20 Ω cm) Si(001) substrates. To prepare the Si wafers for deposition, we first degreased them in ultrasonic baths of acetone then methanol, followed by a soaking in a 1:1:5 solution of $NH_4OH/H_2O_2/H_2O$ at 75 ºC. The wafers were rinsed in deionized water and blown dry with nitrogen. The oxide was removed *in situ* by annealing at 800 ºC until a sharp (2×1) surface reconstruction pattern was observed by reflection high energy electron diffraction (RHEED). Auger electron spectroscopy (AES) revealed a contaminant-free Si surface, and atomic force microscopy (AFM) showed that these surfaces have an rms roughness of ~ 5 Å. A 100-nm Si buffer layer was grown at 600 ºC prior to the Mn deposition from a thermal effusion cell. The Mn flux rate was calibrated from Rutherford backscattering spectroscopy (RBS) and x-ray reflectometry (XRR) measurements.

We prepared samples with Mn thicknesses varying from 0.35 to 4 ML, capped by a 10 to 20-nm Si layer. Lippitz et al.[5] have shown that 0.5 ML of Mn (where we define 1 ML = 1.36×10^{19} atoms/m^2) annealed at 450 ºC on Si(001) produces growth of Mn_5Si_3 and MnSi islands. In an attempt to avoid this bimodal growth, we deposited the Mn at a substrate temperature of -15 ºC. For the thinnest sample, the Si cap was grown at 200 ºC, whereas for the thicker Mn layers it was grown at -15 ºC. To examine the effect of post growth annealing on structural ordering and magnetic moment, the samples were annealed for 1 hour at 200 ºC in Ar atmosphere. The 200 ºC temperature was chosen based on XRR study of the structure of amorphous-Si/ 0.5-ML Mn / Si(001): by annealing up to 250 ºC, no significant change in the Mn-Si interfacial roughness was observed. Annealed samples are referred to as 0.5-ML-A, 2-ML-A and 4-ML-A hereinafter. In addition to the described samples, a 5-nm thick single crystal MnSi film was grown on Si(111) by solid phase epitaxy.[22] It served as a reference for MnSi-B20 structure and for the determination of XAFS parameters. XRR measurements provided information on the distribution of the buried Mn layer, the thickest and thinnest of which are shown in Fig. 1. XRR data was fit using Parratt32 software[23] which is based on Parratt's recursion method.[24] The scattering length density (SLD) profiles of the Mn-containing regions of the thinnest samples were divided into slices and modeled with a Gaussian profile, which was found to give the best fit. The insets of Fig. 1 show the SLD of the corresponding fits to the data, which demonstrate that the Mn remains localized at the substrate-cap interface. For the 0.5-ML sample, the full width at half maximum of the Mn distribution is about 2 Å, whereas the 4-ML sample has an estimated roughness of 4 Å. These values are comparable to the substrate roughness of 5 Å estimated from AFM measurements.

2.1 XAFS experiments and analysis

To investigate the local crystallographic order around Mn atoms, polarization-dependent XAFS spectra were collected in fluorescence mode at the Mn K-edge. The measurements were carried out using facilities of the PNC/XSD ID beamline[25] at the Advanced Photon Source, sector 20. A Mn foil was simultaneously monitored for energy calibration and the Si(111) double crystal monochromator was detuned to 80% of maximum peak at an energy $E = 6750$ eV. The x-ray beam was focused to a 5×5 μm^2 spot using Kirkpatrick-Baez mirrors. Samples were aligned with the incident electric field vector within 84º and 5º of the [001] substrate normal for in-plane (ip) and out-of-plane (oop) measurements, respectively. To eliminate Bragg peaks, samples were mounted on a motorized platform for continuous spinning during data collection. The fluorescence intensity was measured using a 4-element Vortex detector with deadtime correction applied. A helium filled ionization chamber was used to determine the incident intensity I_0, used in data normalization. Multiple x-ray absorption $\mu(E)$ scans were measured for each sample and averaged in ATHENA,[26] which was also used for data normalization and background removal. Theoretical unpolarized XAFS models were calculated using FEFF8.2[27] code at the Mn K-edge with input files generated from ATOMS.[26] The extracted $\chi(k)$ were imported into WinXAS[28] where k^2-weighted Fourier transforms were performed using a Gaussian 10% window function over a typical range of $\Delta k = 2.35 - 11.2$ Å^{-1} (Fig. 2). Data were fit in R-space over a range of $1.13 - 2.82$ Å ($1.10 - 3.00$ Å for the MnSi reference sample).

XAFS from the 5-nm MnSi thin film with a B20 crystal structure served as a reference for our fits. The Mn in a B20 structure has a first shell composed of 7 Si neighbors (1 at 2.305 Å, 3 at 2.402Å and 3 at 2.536Å) and second shell with 6 Mn neighbors at 2.796Å. We could not resolve the three separate bond lengths in the first Si shell due to the relatively limited Δk. Therefore we used a single scattering path from the calculated B20 model to fit the 7 Si neighbors of the first shell (Fig. 3). The same B20 model served as a starting structure to fit the in-plane and out-of-plane data for

each of the 0.35 – 4 ML samples. Note that the positions of the peaks in the Fourier transform appear at distances smaller than the actual bond lengths caused by the XAFS interference function, $\chi(k)$, containing a phase shift originating in the scattering of the photoelectrons.

The magnitudes of the k^2-weighted Fourier transform of the XAFS functions, $|FT\;[k^2\;\chi(k)]|$, in Fig.2(b) show a single peak predominantly due to the Mn-Si shell which is phase-shifted to $R \sim 1.9$ Å. However, we needed a second Mn-Mn scattering path to obtain a good fit. The contribution of this second shell is evident in the overlays of Fig. 4, which show a broadening on the high R-range of the main peak when the Mn thickness is increased. Fig. 5 shows fits to the ultrathin samples, with the coordination number, N_i, path length, R_i, and mean square relative displacement, σ_i^2, for the two scattering paths, Mn-Si ($i = 1$), and Mn-Mn ($i = 2$) treated as fitting parameters, with the amplitude reduction factor, $S_0^2 = 0.70$, and the energy shift, $\Delta E_0 = 5.9$ eV, fixed to the values obtained from the MnSi reference. A simultaneous fit to a k^1- and k^2-weighted model reduced the correlation between N_2 and σ_2^2. The uncertainties of the fitting parameters shown in Table I were estimated by the double $\chi^2_{min.}$ method, fixing one parameter and allowing the remaining parameters to float.[29] Although the errors in R_1, which may be representing the centroid of a distribution in nearest-neighbor distances, do not seem sufficiently conservative by this method.

The results of Table I reveal only a subtle difference between the XAFS parameters of the 0.35-ML sample and the 0.5 – 4 ML samples. The difference between the samples is more clearly shown in Fig. 6, which shows a departure of the fit parameters for the 0.35-ML relative to the other samples. In particular, the coordination number $N_{1\text{-ip}}$ of the 0.35-ML sample is more than a standard deviation higher than the other samples and there is no splitting in the in-plane $R_{1\text{-ip}} = 2.365$ Å and out-of-plane $R_{1\text{-oop}} = 2.367$ Å Mn-Si bond lengths. It is unclear why $N_{1\text{-oop}}$ is less than $N_{1\text{-ip}}$, but an $N_{1\text{-ip}} = 7.7 \pm 0.4$ is within error of a coordination $N = 8$. The value obtained for $N_{1\text{-ip}}$ and R_1 for the 0.35-ML

are consistent with the first Si shell of a B2 structure that is pseudomorphic with the Si(001) substrate. The difference between the in-plane, $R_{2\text{-ip}} = 2.79$ Å, and the out-of-plane Mn-Mn distance, $R_{2\text{-oop}} = 2.82$ Å, implies a 2% tetragonal distortion of the unit cell. However, $R_{2\text{-ip}}$ is larger than $a_{Si}/2 = 2.716$ Å, the value expected for a B2 structure that is pseudomorphic with the Si substrate, which suggests that there is a distortion of the Mn sites relative to a tetragonal B2 structure.

The sensitivity of Mn to growth conditions is illustrated by the difference between the structures of the 0.35-ML sample and of the other samples grown with a cold capping layer. In contrast to the 0.35-ML sample, a comparison between the coordination numbers and bond lengths indicates that the 0.5-ML, 0.5-ML-A, 2-ML-A and 4-ML-A samples evolve toward a B20-like structure as the Mn thickness is increased. No significant structural transition is observed as the thickness is increased from 0.5 to 4 ML, nor between the annealed and unannealed 0.5-ML samples. The N_1 is approximately constant as a function of thickness and is within error of the effective coordination number $N_1 = 6.5$ of the MnSi-B20 reference sample. The Mn-Si bond length increases gradually with thickness and reaches a value equal to the average bond length $R_1 = 2.387$ Å for the 4-ML-A sample. Moreover, there is a clear splitting between $R_{1\text{-ip}}$ and $R_{1\text{-oop}}$, indicative of a difference in structure between this set of samples and the 0.35-ML sample. The Mn-Mn bond is also within error of the B20 reference sample. Given the weak second shell of Mn and the strong correlation between N_2 and $\sigma_2{}^2$, we could not determine a value for N_2. Instead, we use the area under the Mn-Mn profile function, $A_{\text{Mn-Mn}}$, as a measure of the relative combined change in N_2 and $\sigma_2{}^2$. XAFS measurements of the as-grown and post-growth annealed 0.5-ML sample show that the annealing mostly affects the Mn-Mn shell, without a noticeable change to the Mn-Si shell. The increase in $A_{\text{Mn-Mn}}$, is due to an increase in the Mn coordination number and/or a decrease in the structural disorder, although the correlation between N_2 and $\sigma_2{}^2$ prevents a separation of these two contributions. However, we interpret the increase in $A_{\text{Mn-Mn}}$ with annealing, and also with increasing

thickness as an indication that the system is being driven towards a more ordered B20 structure. Although the weak presence of the Mn shell and an absence of a peak in the magnitude of the Fourier transform corresponding to the third nearest neighbor shell indicate a significant disorder in the layers. A comparison between the 200 °C annealing temperature with the typical 400 °C temperature used to create MnSi layers on Si(111) with solid phase epitaxy, suggests that the low annealing temperature is partly responsible for the disorder. The poor lattice mismatch between MnSi(001)-B20 and Si(001) is likely another contributing factor. A similar observation was reported for Mn^{+} implanted Si(001) in Ref. [7], where MnSi precipitates with a disordered B20 coordination were achieved after annealing at 337 °C.

By comparing XAFS data of the two sets of samples, it appears that the growth mode of the Si cap affects the location of the Mn adatoms on the Si(001), leading to distinct coordinations of Mn. While DFT calculations[30] and scanning tunneling microscopy (STM) experiments[31] show that the subsurface sites are more favorable for Mn on Si(001), STM measurements on Mn deposited at room temperature show that Mn adatoms are energetically inhibited from populating these sites at room temperature and instead form chains on the surface.[32,33] By depositing the capping layer prior to annealing, we enabled interactions between the surface Mn layer and the deposited Si that leads to the formation of a MnSi-B20 phase. By annealing the sample prior to deposition of the cap, we drive the Mn into the preferred subsurface sites, which leads to the subsequent formation of the B2-like phase with the addition of the Si-cap.

3. Magnetic properties

The magnetic properties of the samples were characterized using a Superconducting Quantum Interference Device (SQUID) magnetometer with longitudinal pick-up coil geometry. The samples

were wedged inside a standard sample holder consisting of a clear plastic straw. Non-uniformities in the straw induced a weak signal in the SQUID. We measured the background remanent magnetic moment from each sample holder at $T = 50$ K, which ranged between 1×10^{-8} and 5×10^{-8} kA m^2. To maximize the signal from the ultrathin samples, 2-4 pieces of each sample with a typical size of 4 mm × 5 mm were loaded together in the sample holder with the [110] along the axis of the magnetic field. This orientation was chosen to maximize the amount of samples that could be loaded into the sample holder.

The moment versus field m-H loops revealed a weak ferromagnetic signal dominated by that of the Si substrate. In order to remove the substrate contribution, we measured the magnetic response of one of the Si wafers that had been cleaned following the same procedures used to clean the substrates. We fit the field dependence of the moment given by:

$$m(H)_{Si(001)} = \chi_D + m_{sat}\, B_j(x) \,,$$

where χ_D is the diamagnetic susceptibility, m_{sat} is the saturation moment and $B_j(x)$ is the Brillouin function. The fit shown in Fig. 7 yielded a total angular momentum quantum number $j = 1.6 \pm 0.2$ consistent with a B^{2+} state in Si,[34] and $m_{sat} = (2.6 \pm 0.2) \times 10^{-5}$ A m^2/kg that corresponds to a boron concentration of 4.2×10^{15} atoms/cm^3. This falls well within the boron concentration range of $1.0 \times 10^{15} - 1.0 \times 10^{16}$ atoms/cm^3 extracted from the substrate resistivity.

There is a clear difference between the magnetic response of the B2-like sample compared to that of the B20-like samples. In Fig. 8 we show the m-H loops of the 0.35-ML and 4-ML-A samples measured at $T = 2$ K, which all show a remanent moment indicative of long-range magnetic order. The 0.35-ML sample, with the B2-like structure, has a saturation field $\mu_0\, H_{sat} = 0.12$ T and a coercive field of approximately 10 mT (inset of Fig. 8(a)). We extrapolate the linear high field

portion of the m - H curves above a field of 1 T to zero field in order to obtain a moment of 0.33 μ_B/Mn for the B2-like sample. In contrast, the m-H loops of the B20-like structures are more rounded with a much higher $\mu_0 H_{sat}$ = 1.8 T and a larger coercive field, which is $\mu_0 H_c$ = 35 mT in the case of the 4-ML-A sample. The fact that H_c is much larger than the 5 mT coercive field of B20-MnSi / Si(111) [22] is consistent with the large disorder inferred from the XAFS fits.

There is a dramatic difference between the Curie temperatures of the B2- and B20-like structures. Due to the large susceptibility of the substrate, the clearest estimates of the T_C come from measurements of the remanent moment, m_r, where there is no substrate contribution. We measure m_r following saturation in a 5-T field at T = 2 K and estimate T_C from the point where m_r goes to zero in Fig. 9. For the B20-like structures, the estimated T_C drops with increasing thickness: T_C = 18 K for the 0.5-ML-A sample, T_C = 13 K for the 2-ML-A and T_C = 4 K for the 4-ML-A sample. These low values for T_C are expected from a B20 structure, where the bulk T_C is only 29.5 K. A combination of finite-size effects[35] and the influence of defects[22] accounts for the difference between the ultrathin film measurements and bulk. However, the origin of the drop in T_C with thickness is not clear. These low Curie temperatures are in stark contrast to the B2-like sample, which shows a slow linear decay of m_r that reaches the background moment of the sample at a temperature above 250 K, which is in reasonably good agreement with the predictions of Ref. [18].

Our study is consistent with the observation in the literature that the structure of dilute Mn_xSi_{1-x} alloys is very sensitive to growth conditions. The growth temperature of the Si-capping influences the local chemical environment of the Mn atoms. We also find that the magnetic properties are equally sensitive to the chemical structure. The SQUID data suggest a correlation between the magnetism and the Mn-Mn shell. An increase in A_{Mn-Mn} due to annealing is correlated with the increase in m_{sat}, as shown in Fig. 10. The largest increase is observed for the thinnest sample presumably because it experiences a larger influence from the single crystal substrate, as

compared to the thicker samples whose chemistry may be more strongly affected by the disordered amorphous cap. For the 0.5-ML sample an increase in $A_{Mn\text{-}Mn}$ from 10 % to 13.5 % after annealing coincides with an increase in the moment from 0.09 μ_B/Mn to 0.26 μ_B/Mn.

Some insight into the magnetic structure of the B20-like films can be obtained from the thickness dependence of the saturated moment shown in Fig. 10. The moment drops from 0.26 μ_B / Mn, to approximately 0.05 μ_B/Mn between 2 and 3 ML before it increases again at 4 ML. A similar non-monotonic thickness dependence is observed for MnSi / Si(111) films,[22] and is explained in part by the results of DFT calculations that predict an enhanced interfacial moment.[36] The drop seen in the 2- and 3-ML films is then attributed in part to the formation of bulk moments, and due to the presence of defects, which possibly explain the decrease in the moment of MnSi / Si(111) films.[22] A second possibility is the formation of an antiferromagnetic state. For MnSi/Si(111), a magnetic configuration with large uncompensated interfacial moments that are antiparallel to smaller central moments is found to be nearly degenerate with the ferromagnetic state.[22] The drop in magnetic moment could possibly be due to the formation of anti-parallel spins in the interior of the film. The more ordered 4-ML film has a higher moment presumably due to fewer defects and a more highly coordinated Mn shell.

4. Conclusion

Our XAFS results show that it is possible to stabilize a disordered metastable MnSi-B2-like structure on Si(001) under appropriate growth conditions. Two different local environments for Mn are found that depend on whether the Mn layer was annealed prior to deposition of the Si cap, or post-cap deposition. The magnetic properties of the studied samples are shown to be highly sensitive to the Mn coordination, with a possibly stronger influence from the Mn-Mn shell. The B2-like structure has a magnetic moment of 0.33 μ_B/Mn, and exhibits a ferromagnetic ordering with a T_C

above 250 K that is substantially larger than the largest estimated $T_C = 18$ K for samples with MnSi-B20 structure.

References

1- M. Bolduc, C. Awo-Affouda, A. Stollenwerk, M. B. Huang, F. G. Ramos, G. Agnello, and V. P. LaBella, Phys. Rev. B **71**, 033302 (2005).

2- F. M. Zhang, X. C. Liu, J. Gao, X. S. Wu, Y. W. Du, H. Zhu, J. Q. Xiao, and P. Chen, Appl. Phys. Lett. **85**, 786 (2004)

3- C. Awo-Affouda, M. Bolduc, M. B. Huang, F. Ramos, K. A. Dunn, B. Thiel, G. Agnello, and V. P. LaBella, J. Vac. Sci. Technol. A **24**, 1644 (2006)

4- V. Ko, K. L. Teo, T. Liew, T. C. Chong, M. MacKenzie, I. MacLaren, and J. N. Chapman. J. Appl. Phys. **104**, 033912 (2008).

5- H. Lippitz, J. J. Paggel, and P. Fumagalli, Surf Sci **575**, 307 (2005).

6- A. Orlov, A. Granovsky, L. Balagurov, *et al*, Journal of Experimental and Theoretical Physics **109**, 602 (2009).

7- A. Wolska, K. Lawniczak-Jablonska, M. Klepka, M. S. Walczak, and A. Misiuk, Phys.Rev.B **75**, 113201 (2007).

8- S. Zhou, K. Potzger, G. Zhang, *et al*, Phys.Rev.B **75**, 085203 (2007).

9- Y. Zhang, Q. Jiang, D. J. Smith, and J. Drucker, J. Appl. Phys. **98**, 033512 (2005).

10- G. I. Kalishevich, Yu. A. Vereshagin, and P. V. Gel'd, Sov. Phys. Solid State **16**, 1151 (1974)

11- S. Tomiyoshi and H. Watanabe, J. Phys. Soc. Jpn. **39**, 295 (1975)

12- A. Z. Menshikov, A. P. Vokhmyanin, and Y. A. Dorofeev, physica status solidi (b) **158**, 319 (1990).

13- Y. Ishikawa, K. Tajima, D. Bloch, and M. Roth, Solid State Commun **19**, 525 (1976).

14- T. Nakajima and J. Schelten, J Magn Magn Mater **21**, 157 (1980).

15- U. Gottlieb, A. Sulpice, B. Lambert-Andron, and O. Laborde, J. Alloys Compounds **361**, 13 (2003).

16- V. N. Men'shov, V. V. Tugushev, S. Caprara, and E. V. Chulkov, Phys.Rev.B **83**, 035201 (2011).

17- H. Wu, M. Hortamani, P. Kratzer, and M. Scheffler, Phys. Rev. Lett. **92**, 237202 (2004).

18- M. Hortamani, L. Sandratskii, P. Kratzer, I. Mertig, and M. Scheffler, Phys.Rev.B **78**, 104402 (2008).

19- S. Walter, F. Blobner, M. Krause, S. Müller, K. Heinz, and U Starke, J. Phys.: Condens. Matter **15,** 5207 (2003)

20- H. von Känel, C. Schwarz, S. Goncalves-Conto, E. Müller, L. Miglio, F. Tavazza, and G. Malegori, Phys. Rev. Lett. **74**, 1163 (1995).

21- Q. F. Xiao, S. Kahwaji, T. L. Monchesky, R. A. Gordon, and E. D.Crozier, J. Phys. Conf. Series **190**, 012101 (2009).

22- E. Karhu, S. Kahwaji, T. L. Monchesky, C. Parsons, M. D. Robertson, and C. Maunders, Phys.Rev.B **82**, 184417 (2010).

23- C. Braun, PARRATT32 program [Berlin: Berlin Neutron Scattering Center (BENSC), Hahn-Meitner Institut].

24- L. G. Parratt, Phys. Rev. **95**, 359 (1954).

25- S. M. Heald, D. L. Brewe, E. A. Stern, K. H. Kim, F. C. Brown, D. T. Jiang, E. D. Crozier, and R. A. Gordon, J. Synchrotron Rad. **6**, 347 (1999).

26- B. Ravel and M. Newville, J. Synchrotron Rad. **12**, 537 (2005).

27- A. L. Ankudinov, B. Ravel, J. J. Rehr, and S. D. Conradson, Phys.Rev.B **58**, 7565 (1998).

28- T. Ressler, J. Physique IV **7,** C2-269 (1997).

29- D. T. Jiang, E. D. Crozier, and B. Heinrich, Phys. Rev. B **44,** 6401 (1991); F. W. Lytle, D. E. Sayer, and E. A. Stern, Physica B **158,** 701 (1989).

30- M. Hortamani, H. Wu, P. Kratzer, and M. Scheffler, Phys.Rev.B **74**, 205305 (2006).

31- M. R. Krause, A. J. Stollenwerk, J. Reed, V. P. LaBella, M. Hortamani, P. Kratzer, and M. Scheffler, Phys.Rev.B **75**, 205326 (2007).

32- C. A. Nolph, H. Liu, and P. Reinke, Surf Sci **605**, L29 (2011).

33- J. T. Wang, C. Chen, E. Wang, and Y. Kawazoe, Phys. Rev. Lett. **105**, 116102 (2010).

34- M. P. Sarachik, D. R. He, W. Li, M. Levy, and J. S. Brooks, Phys.Rev.B **31**, 1469 (1985).

35- M. E. Fisher and M. N. Barber, Phys. Rev. Lett. **28**, 1516 (1972).

36- M. Hortamani, P. Kratzer, and M. Scheffler, Phys.Rev.B **76**, 235426 (2007).

Table I. XAFS parameters obtained from the fit of the in-plane (ip) and out-of-plane (oop) data of the samples and ip data of the MnSi-B20 reference. The percent fit residual (R%) is included along with the uncertainty of each fitting parameter (in parentheses). $A_{\text{Mn-Mn}}$ refers to the area under the Mn-Mn profile function relative to that of Mn-Si. S_0^2 is fixed to 0.70 ± 0.02.

Sample	ΔE_0 (eV)	N_1 (Si)	R_1 (Å)	σ_1^2 (Å²)	$A_{\text{Mn-Mn}}$ (%)	R_2 (Å)	R (%)
MnSi-B20 ref.	5.9(6)	6.5	2.39(1)	0.010(4)	100	2.788(6)	1.88
0.35-ML_ip	5.9	7.7(4)	2.365(2)	0.0096(8)	9.2	2.79(1)	0.47
0.35-ML_oop	5.9	7.0(6)	2.367(4)	0.008(1)	13.2	2.82(2)	0.82
0.5-ML_ip	5.9	7.0(4)	2.363(2)	0.0097(7)	10.5	2.78(1)	0.84
0.5-ML_oop	5.9	7.1(5)	2.375(3)	0.0097(9)	9.4	2.81(1)	1.07
0.5-ML-A_ip	5.9	6.6(9)	2.363(6)	0.009(2)	14.2	2.79(3)	2.35
0.5-ML-A_oop	5.9	6.9(3)	2.372(2)	0.0094(6)	13.0	2.78(1)	0.48
2-ML-A_ip	5.9	6.9(4)	2.371(3)	0.0092(7)	14.8	2.81(1)	1.09
2-ML-A_oop	5.9	6.8(7)	2.381(4)	0.010(2)	14.1	2.80(2)	0.85
4-ML-A_ip	5.9	6.2(4)	2.384(3)	0.010(1)	18.5	2.78(1)	0.92
4-ML-A_oop	5.9	6.4(7)	2.391(5)	0.011(2)	17.3	2.77(3)	0.78

Figures Captions

Fig. 1. (Color online) Simulations (solid red line) of XRR spectra (open circles) of as-grown 0.5-ML and 4.0-ML MnSi samples. The scattering length density (SLD) profiles in the insets show that Mn remains at the interface.

Fig. 2. (Color online) (a) k^2-weighted XAFS interference functions of MnSi/Si(001) and the reference 5nm MnSi-B20/Si(111) samples and (b) the corresponding k^2-weighted Fourier transform (FT) magnitudes. A Gaussian 10% window function over a typical range of 2.35 – 11.2 Å^{-1} was used in FT. Both in-plane (solid lines) and out-of-plane (blue dashed lines) measurements are shown.

Fig. 3. (Color online) Open circles: k^2-weighted Fourier transform magnitude of the reference MnSi-B20 sample. Solid line (red): fit to the data. Dashed lines (blue): fitting range in R-space

Fig. 4. (Color online) Overlays of k^2-weighted Fourier transform magnitudes of the out-of-plane XAFS data of the measured samples. A broadening is observed above R~2.5 Å as Mn thickness is increased.

Fig. 5. (Color online) Fit to XAFS data of samples 0.35-ML and 4ML-A. (a) and (b) show the profile functions of Mn-Si and Mn-Mn scattering paths that were combined to obtain the final fits shown in (c) and (d).

Fig. 6. (Color online) XAFS fitting parameters as a function of Mn thickness. (a) Parameters of first Mn-Si shell and (b) parameters of the second Mn-Mn shell. Squares (circles) refer to in-plane (out-

of-plane) data and open symbols refer to non-annealed 0.5-ML sample. Solid (green) horizontal line corresponds to the MnSi-B20 reference with the associated uncertainty indicated by the dashed lines.

Fig. 7. (Color online) Magnetic moment versus applied field of a Si(001) substrate after subtraction of the diamagnetic contribution from the measured data (shown in inset). A Brillouin function fit to one branch is used to extract the paramagnetic contribution of the substrate.

Fig. 8. Hysteresis loops of (a) the 0.35-ML sample (area =0.45cm^2) and (b) the 4-ML-A sample (area =1.07cm^2) measured at T=2 K. Background from the Si substrate has been subtracted. Insets show the coercive field H_c of each sample. The shape of the loop in (b) is representative of all as-grown and annealed 0.5ML - 4ML samples. Note that the "jump" in the moment seen in the top branch in (a) is an instrumental artifact caused by a change in the emu-range during measurement as discussed in A. Ney, T. Kammermeier, V. Ney, K. Ollefs, and S. Ye, J Magn Magn Mater **320**, 3341 (2008).

Fig. 9. Remanent moment, m_r, as a function of temperature for (a) 0.35-ML, (b) 0.5-ML-A, (c) 2-ML-A and (d) 4-ML-A samples. T_C is estimated from the point where m_r drops to a minimum.

Fig. 10. (Color online) Mn magnetic moment as a function of thickness. The magnetic moment of samples with B20-like structure generally increases after annealing at 200 ºC. Same trend is observed for as-grown and annealed samples as Mn thickness increases from 0.5 to 4 ML.

Fig. 1.
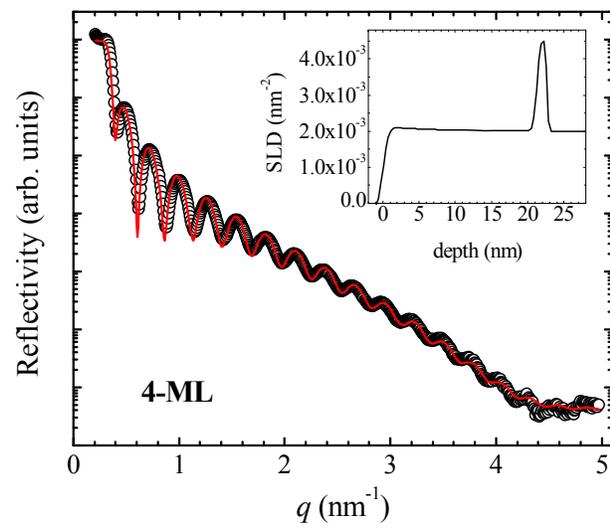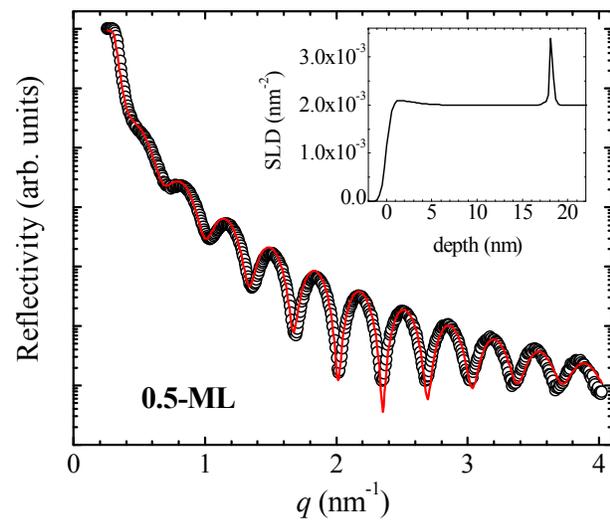
Fig. 2.
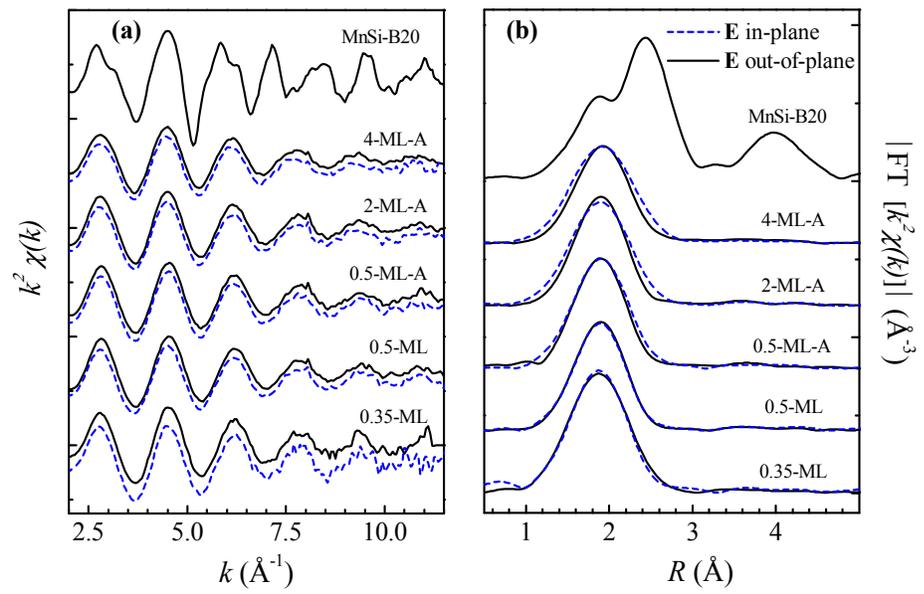
Fig. 3.
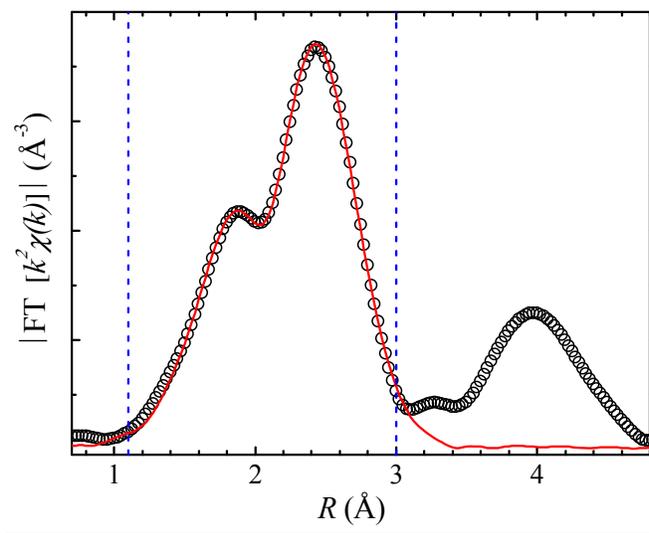
Fig. 4.
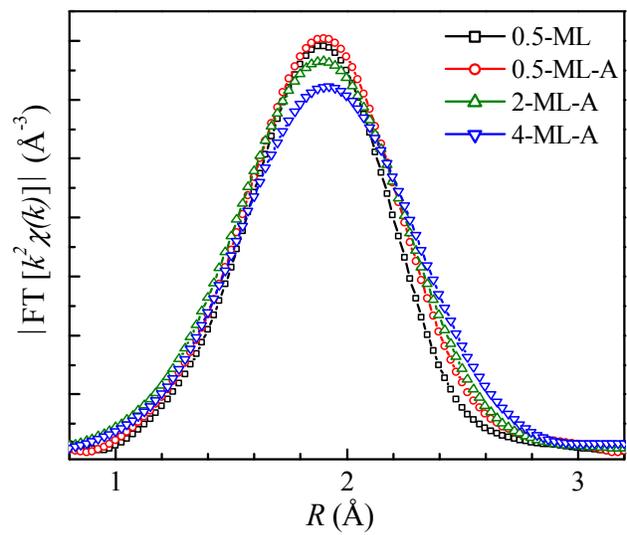
Fig. 5.
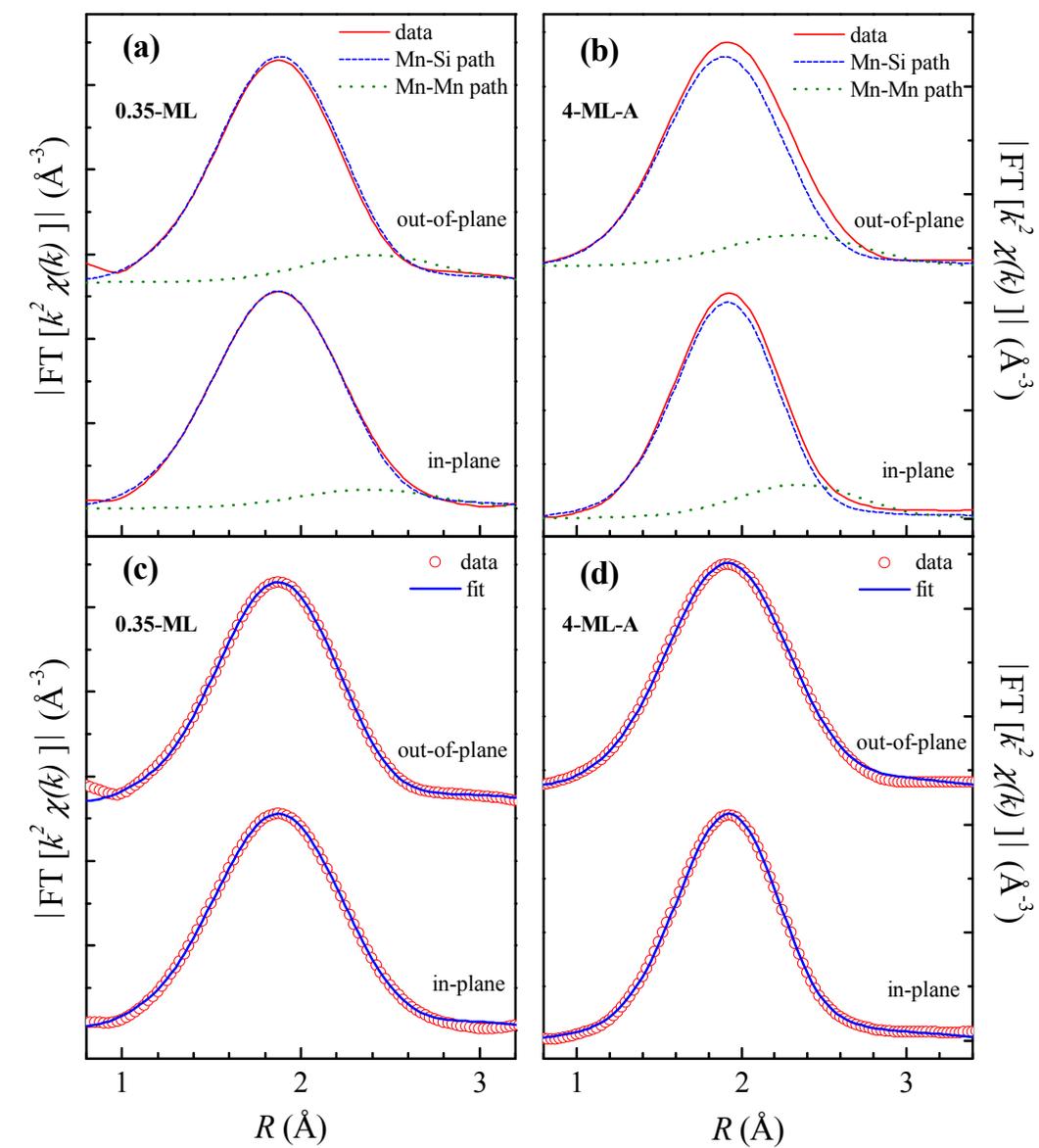
Fig. 6.

Fig. 7.

Fig. 8.

Fig. 9.

Fig. 10.